crystals

MDPI

Article

Epitaxial Orientation Transfer and Interfacial Stray-Grain Formation During Heterogeneous Seeding of DD419 Single-Crystal Superalloy with Ni-20W Seeds

Xiaoyi Gong [1,2], Min Lu [1], Chen Chen [3,*], Yunxing Zhao [2], Dexin Ma [1,2,*], Jianhui Wei [1,2], Weitai Xu [2], Lv Li [2] and Yangpi Deng [2]

[1] Powder Metallurgy Research Institute, Central South University, Changsha 410083, China
[2] Shenzhen Wedge Aviation Technology Co., Ltd., Shenzhen 518045, China
[3] Hunan Key Laboratory of Welding Process Technology, Hunan Mechanical & Electrical Polytechnic, Changsha 410151, China
* Correspondence: chenchenfire@163.com (C.C.); madexin@csu.edu.cn (D.M.)

Abstract

Ni-W alloys are promising heterogeneous seed materials for directional solidification of Ni-based single-crystal superalloys. In this study, Ni-20 wt.% W (Ni-20W) seeds were used to initiate DD419 castings. Their solidification characteristics, melt-back behavior, interfacial microstructure, and orientation transfer were compared with those of DD419 homogeneous seeds. In two thermal cycles, Ni-20W had liquidus temperatures of 1492.6 and 1493.6 °C, with a critical nucleation undercooling of 14.5 °C in both cycles. DD419 had liquidus temperatures of 1388.8 and 1394.1 °C and undercoolings of 44 and 37 °C, respectively. Metallography and paired Laue measurements of one plate casting were consistent with orientation inheritance from Ni-20W to DD419. The software-reported differences in Theta and Alpha were 0.2° and 2.7°, respectively; the software-reported R value was 3.52. In the same-batch turbine-blade comparison, visible interfacial stray grains were observed on the examined starter-region surfaces of all six Ni-20W-seeded blades. No comparable features were observed on the examined surfaces of the three DD419 homogeneous-seeded blades. The maximum observed melt-back lengths were approximately 12 mm for Ni-20W and 45 mm for DD419. These observations indicate that orientation inheritance in the plate specimen did not ensure a defect-free starter region in the blade comparison. The two seed materials also showed markedly different melt-back behavior under the same nominal casting schedule.

Keywords: single-crystal superalloy; heterogeneous seed; Ni-20W alloy; epitaxial growth; orientation transfer; stray grain; seed-casting interface

Academic Editor: Yuying Wu

Received: 14 September 2026
Revised: 1 November 2026
Accepted: 3 November 2026
Published: 4 November 2026

Copyright: © 2026 by the authors. Licensee MDPI, Basel, Switzerland. This article is an open access article distributed under the terms and conditions of the Creative Commons Attribution (CC BY) license.

1. Introduction

Ni-based single-crystal superalloys are widely used in turbine blades exposed to severe high-temperature conditions. The absence of high-angle grain boundaries improves their high-temperature mechanical performance and structural reliability. During investment casting, single-crystal structures are generally produced using either grain-selection or seeding techniques. Spiral grain selectors are widely used because they are simple and reliable. However, they do not precisely control the primary crystallographic orientation

and offer little direct control over the secondary orientation [1–4]. In contrast, the seeding method enables a predefined crystallographic orientation to be transferred from a seed crystal to the casting and is therefore attractive for components requiring strict three-dimensional orientation control.

Conventional single-crystal seeding generally employs homogeneous seeds with compositions identical or similar to that of the cast alloy. Their performance depends strongly on alloy chemistry, seed-mold interaction, and the thermal history imposed during seed melt-back. Inadequate melt-back, residual-solid morphology, and transient interfacial conditions can promote stray grains or other crystallographic discontinuities near the seed-casting transition [5–9]. Consequently, controlling the melt-back region remains a central problem in seed-assisted directional solidification.

Ni-W alloys were proposed as heterogeneous seed materials to reduce problems associated with the broad partially melted regions of multicomponent superalloy seeds [10]. Studies of Ni-W single crystals have shown cellular or cellular-dendritic morphologies whose development depends on composition and growth conditions [11–14]. Earlier seeding studies examined solidification and fusion-zone behavior in superalloy systems, including low-segregation heterogeneous seeds [15,16]. More recently, Qin et al. directly characterized the remelting interface of Ni-W heterogeneous seeds under different solidification conditions and related the interfacial morphology to constitutional undercooling and the local thermal gradient [17].

Recent studies have also identified other mechanisms of stray-grain formation during seeding. In DD419 homogeneous seeding, a seed-mold gap can generate a chilled layer and associated stray grains [18], while oxide films have been shown to obstruct orientation transfer and promote additional grain formation in a superalloy seeding system [19]. Transient thermal evolution within the seed region [20] and oxygen-related heterogeneous nucleation in single-crystal castings [21] further illustrate the multi-factorial nature of stray-grain formation. Separately, lower undercooling capacity has been associated with higher stray-grain susceptibility in Ni-based single-crystal superalloys [22], while epitaxial growth from a partially unmelted seed remains the crystallographic basis of orientation transfer [23].

These studies establish several important mechanisms. However, they do not directly address how Ni-20W heterogeneous seeds and DD419 homogeneous seeds compare under the same blade-casting schedule, or whether orientation inheritance from Ni-20W to DD419 ensures a defect-free interface. The present work therefore combines thermal analysis, plate-based evidence of orientation transfer, and a same-batch blade comparison of melt-back and interfacial stray-grain behavior.

Ni-20 wt.% W heterogeneous seeds were prepared by the spiral grain-selection method and used for seeding of DD419 single-crystal superalloy castings. The liquidus temperature and critical nucleation undercooling of both alloys were measured first. Plate-casting experiments were then used to examine the seed-casting interface and crystallographic orientation transfer. Ni-20W heterogeneous seeds and DD419 homogeneous seeds of different heights were also compared in the same turbine-blade casting batch.

2. Materials and Methods

2.1. Materials and Preparation of Ni-20W Seeds

The materials investigated in this study were a Ni-20 wt.% W binary alloy and the DD419 Ni-based single-crystal superalloy. Their nominal chemical compositions are listed in Table 1. The Ni-20W alloy was prepared by mixing Ni and W at a mass ratio of 80:20, followed by melting in a vacuum induction furnace.

Ni-20W seed crystals were produced by the spiral grain-selection method. Alumina ceramic shells were prepared for seed production, plate casting, and turbine-blade casting.

https://doi.org/10.3390/cryst16110705

Directional solidification was performed in a VIM-IC/DS/SC vacuum directional-solidification furnace manufactured by ALD. For seed preparation and casting, the furnace set point and alloy pouring temperature were both 1520 °C, and the withdrawal rate was 3 mm/min. After directional solidification, the ceramic shells and gating systems were removed, and the castings were macroetched to assess single-crystal integrity.

All prepared Ni-20W seeds were inspected by macroetching. Only macroscopically intact single-crystal sections without visible stray grains were selected for the subsequent plate and turbine-blade seeding experiments. Regions containing visible stray grains were excluded.

Table 1. Nominal chemical compositions of the Ni-20W and DD419 alloys (wt.%).

Alloy	Cr	Co	W	Mo	Al	Ti	Ta	Re	Nb	Hf	Ni
Ni-20W	–	–	20.00	–	–	–	–	–	–	–	Balance
DD419	6.38	9.48	6.37	0.61	5.82	0.98	6.57	2.82	0.02	0.09	Balance

2.2. Measurement of Solidification Parameters

The liquidus temperature, critical nucleation temperature, and critical nucleation undercooling of Ni-20W and DD419 were measured using the thermal-analysis method reported previously [24]. Thermocouples were embedded in both alloys to continuously record temperature during heating, melting, cooling, and solidification. Two complete thermal cycles were performed for each alloy to compare the measurements between cycles.

The liquidus temperature, T_L, was determined from the thermal response during melting, whereas the critical nucleation temperature (T_N) was identified from the recalescence behavior during cooling. The critical nucleation undercooling was calculated as follows:

$$\Delta T_N = T_L - T_N$$

2.3. Plate-Casting Seeding Experiment

Plate-casting experiments were conducted using Ni-20W heterogeneous seeds to evaluate their ability to transfer crystallographic orientation to DD419. The Ni-20W seed had a total length of 45 mm. The assembly schematic shows 30 mm of the seed below the lower shell opening and the remaining 15 mm extending into the casting region (Figure 1). DD419 was used as the casting alloy. Two plate castings were prepared.

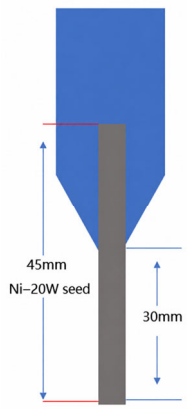


Figure 1. Plate-casting seed placement based on the original assembly drawing.

Following directional solidification and shell removal, the plate castings were macroetched to examine their overall grain structure and the integrity of the seeding region. The seeding region was then sectioned longitudinally to examine the seed-casting interface and the adjacent microstructure.

2.4. Comparative Turbine-Blade Seeding Experiments

To compare heterogeneous and homogeneous seeds under the same nominal casting schedule, Ni-20W heterogeneous seeds and DD419 homogeneous seeds were placed in the same mold and used to produce DD419 turbine-blade castings. Seed heights of 30, 40, and 50 mm were investigated for each seed material. Two Ni-20W-seeded blades and one DD419-seeded blade were cast at each height, giving nine blade castings in a single comparative batch. The mold was positioned at the center of the furnace, providing a common furnace setup for both seed types. Although the mold was positioned at the center of the furnace, the relative positions of the two seed types within the mold and the local thermal conditions at their respective positions were not documented. Therefore, possible positional effects cannot be ruled out.

After casting and shell removal, the blades were macroetched and examined visually for grain defects. The examination focused on the starter region and on stray grains near the seed-casting transition region. All nine blade castings were examined. The detached seed portions were sectioned longitudinally to assess melt-back behavior and the remaining seed morphology.

2.5. Microstructural and Crystallographic Characterization

Cross-sectional and longitudinal specimens were cut from the seed and seeding regions using wire electrical-discharge machining. The specimens were ground, polished, and chemically etched before metallographic examination using a Nikon MM-400 optical microscope (Nikon Corporation, Tokyo, Japan).

One of the two plate castings was randomly selected for paired Laue measurements using a Proto Laue X-ray diffraction system. The crystallographic orientations of the Ni-20W seed and the corresponding DD419 casting were measured, and the software-reported Theta, Alpha, and R values were recorded.

3. Results and Discussion

3.1. Microstructure and Solidification Characteristics of Ni-20W Seeds

Figure 1 shows the macroscopic appearance of the Ni-20W seeds after shell removal and macroetching. The seeds were visibly bent after shell removal, indicating their susceptibility to deformation under the processing and handling conditions used here. Macroetching revealed visible stray-grain defects on some seed surfaces in the seed-preparation batch (Figure 2(b1–b3)), as indicated by the red arrows. This observation highlights the need for careful control of directional-solidification conditions when preparing Ni-20W seeds.

The transverse microstructure of the Ni-20W seed is shown in Figure 3. A regular directional-solidification structure was observed at low magnification. In transverse section, the features appeared cellular-like to weakly dendritic. At higher magnification, small bright-contrast regions were visible between some solidification features. Previous studies have reported W partitioning during solidification in Ni-based alloys [25,26]. Such solute redistribution may be relevant to the observed microstructural contrast; however, the available optical micrographs do not establish whether these regions are W-enriched or identify their phase. Further SEM-EDS analysis could help clarify their local composition.

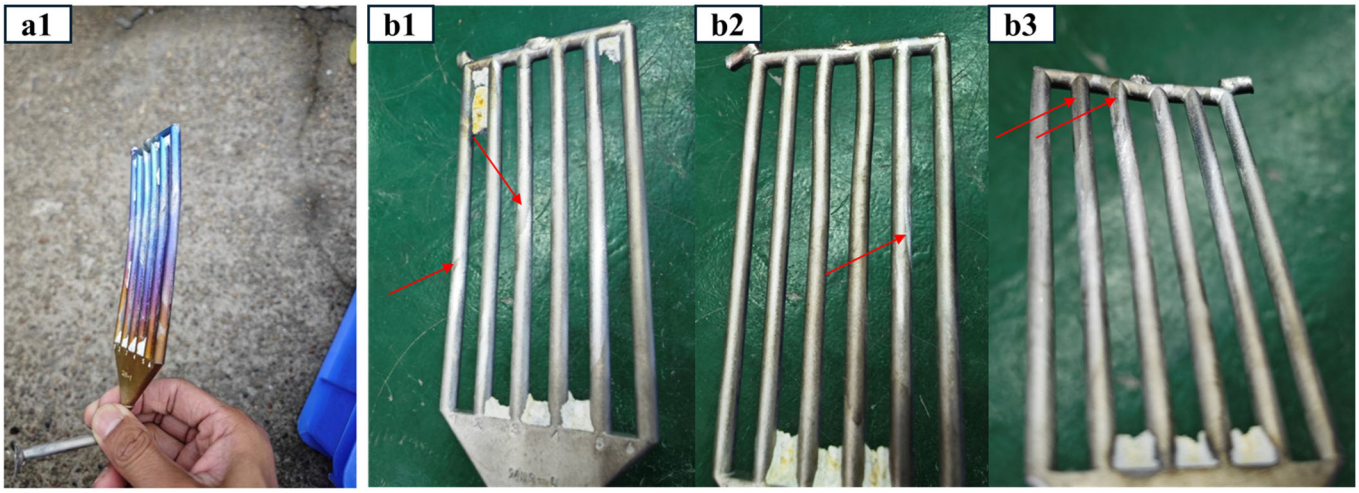


Figure 2. Macroscopic appearance of directionally solidified Ni-20W seeds: (**a1**) after shell removal; ((**b1**)–(**b3**)) three groups of macroetched seeds from the same seed-preparation casting batch. Red arrows indicate representative surface regions identified during macroetching as showing stray-grain defects. Regions showing these defects were excluded from subsequent seeding experiments.

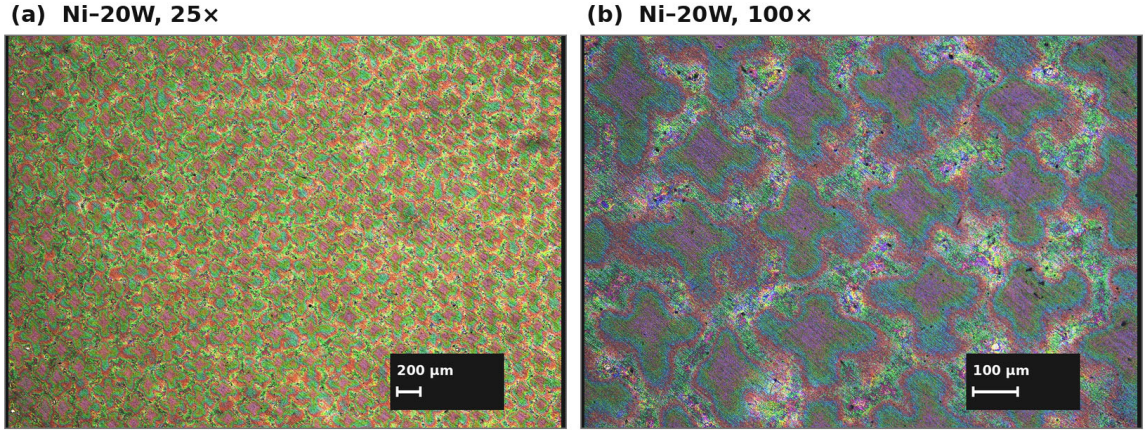


Figure 3. Optical micrographs of the directionally solidified Ni-20W seed: (**a**) transverse microstructure at 25× magnification; (**b**) higher-magnification transverse view at 100× showing cellular-dendritic features and bright-contrast regions.

The thermal responses of Ni-20W and DD419 during two heating-cooling cycles are compared in Figure 4. For Ni-20W, the liquidus temperatures were 1492.6 and 1493.6 °C, while the corresponding critical nucleation temperatures were 1478.1 and 1479.1 °C. The critical nucleation undercooling was therefore 14.5 °C in both cycles. In contrast, DD419 exhibited liquidus temperatures of 1388.8 and 1394.1 °C and critical nucleation undercoolings of 44 and 37 °C, respectively.

Two differences are relevant to heterogeneous seeding. First, the liquidus temperature of Ni-20W was about 100 °C higher than that of DD419 under the measurement conditions used here. This suggests that greater thermal exposure may be needed to achieve a comparable degree of melt-back. Second, Ni-20W exhibited a substantially lower critical nucleation undercooling. Previous work has linked lower undercooling capacity in Ni-based single-crystal superalloys to a greater tendency for stray-grain formation [22]. These values were measured using bulk thermal-analysis specimens and do not directly characterize the liquid near the Ni-20W/DD419 interface.

3.2. Seed-Casting Interface and Epitaxial Growth of DD419 on the Ni-20W Seed

Figure 5 shows the macroetched DD419 plate castings produced using Ni-20W heterogeneous seeds. Most of each casting retained a single-crystal morphology, indicating that the Ni-20W seeds could initiate and sustain oriented growth in DD419. However, visible stray-grain features were observed near the seed-casting transition region. In one casting, a feature extended upward from the side of the seeding region.

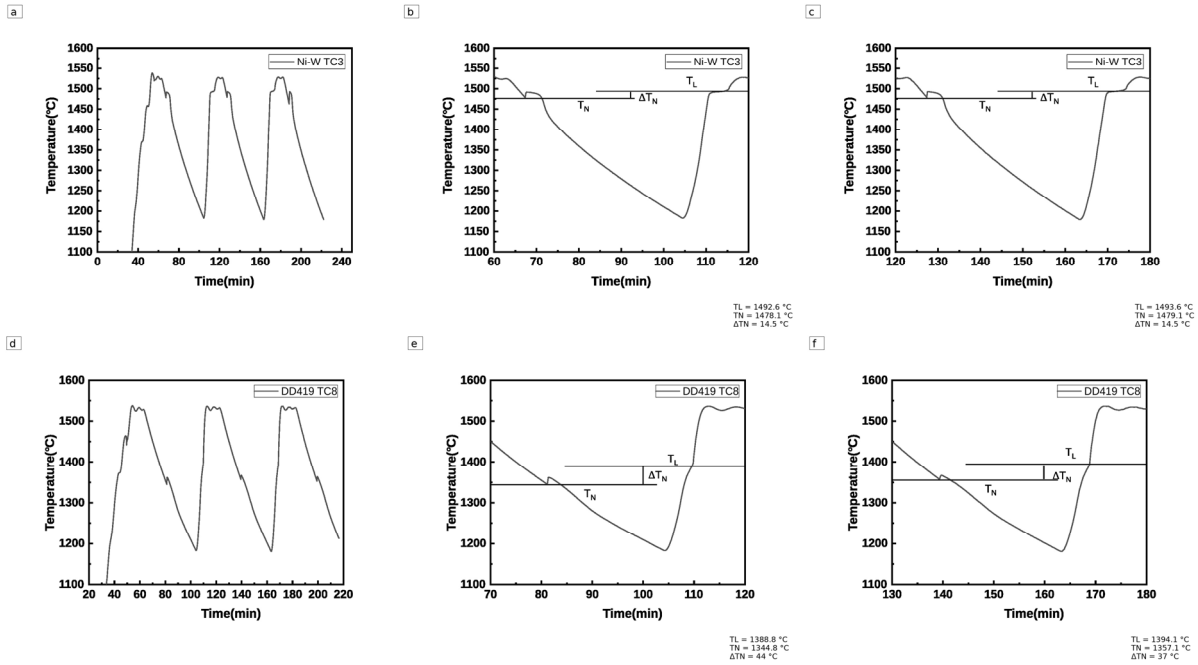


Figure 4. Thermal-analysis curves of Ni-20W and DD419 used to determine the liquidus temperature (T_L), critical nucleation temperature (T_N), and critical nucleation undercooling (ΔT_N): (**a**) thermal cycles of Ni-20W; (**b**,**c**) enlarged curves for cycles 1 and 2 of Ni-20W; (**d**) thermal cycles of DD419; (**e**,**f**) enlarged curves for cycles 1 and 2 of DD419.

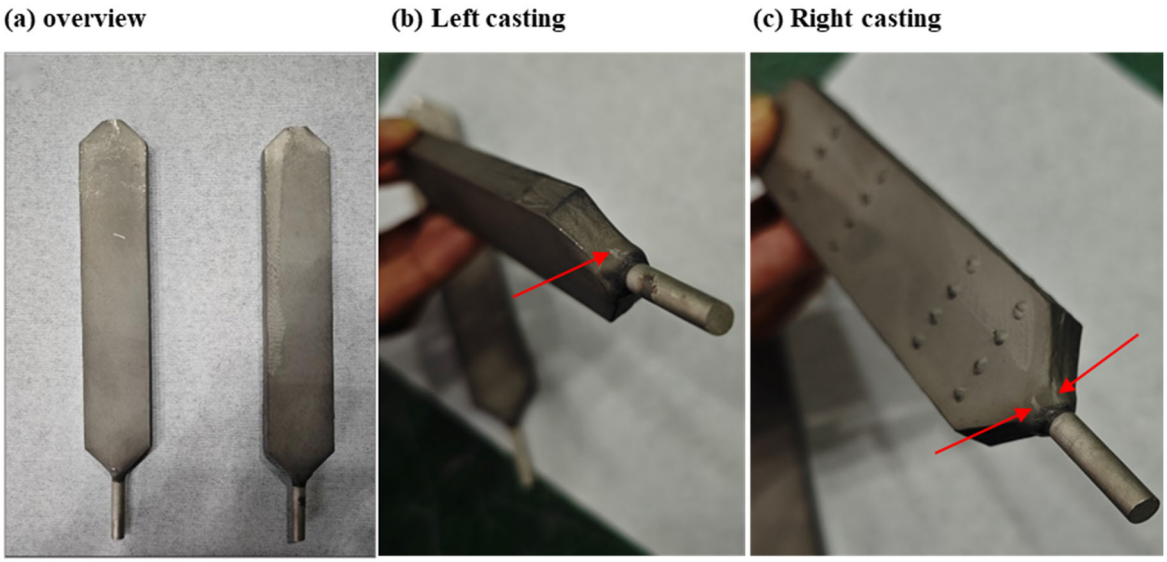


Figure 5. Macroetched DD419 plate castings produced using Ni-20W heterogeneous seeds: (**a**) overall grain morphology of the seeded castings; (**b**) local seed-casting transition region of the left plate in (**a**); (**c**) corresponding region of the right plate in (**a**). Surface macroetching reveals contrasting

local features; individual grain orientations were not measured. Red arrows identify the local seed-adjacent features indicated in the original laboratory photographs.

Figure 6 shows the longitudinal microstructure of the seeding region. A distinct interface separated the lower Ni-20W seed from the upper DD419 casting. The seed-casting interface appeared relatively flat in the observed area. Above the interface, the DD419 casting showed a clear dendritic morphology. The original dendritic pattern in the Ni-20W seed became less distinct near the interface. Fine solidification features immediately above the interface subsequently developed into the dendritic structure of the DD419 casting.

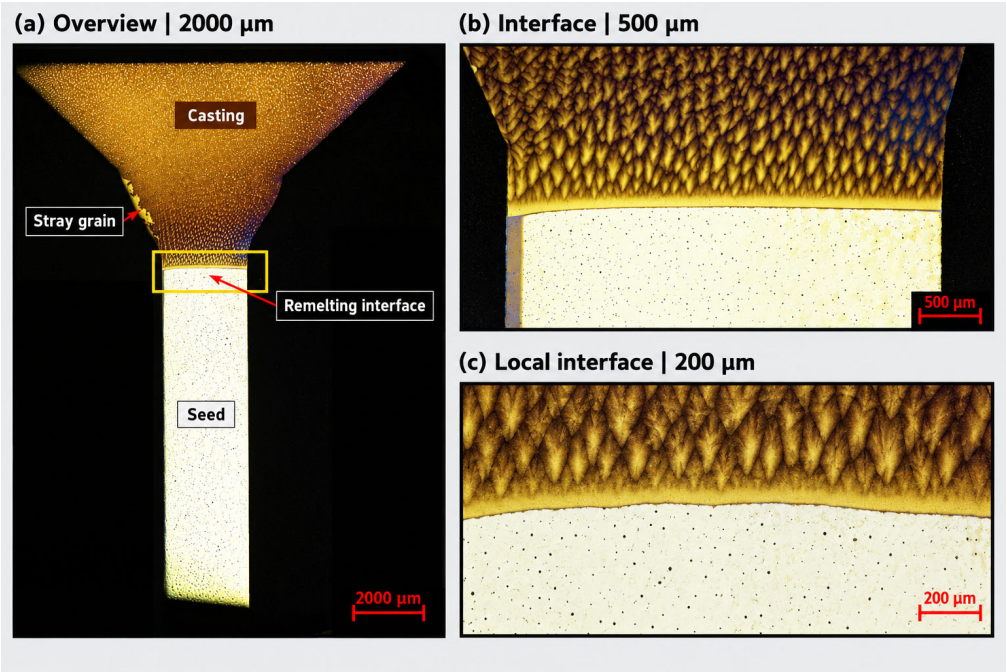


Figure 6. Optical micrographs of the longitudinal seeding region between the Ni-20W seed and DD419 casting: (**a**) overall microstructure of the seeding region; (**b**) seed-casting interface between the Ni-20W seed and DD419 casting; (**c**) higher-magnification view of the local interface. The outlined band in (**a**) identifies the general interface vicinity, rather than the exact fields of view of (**b**,**c**).

The continuity of the microstructure across the interface is consistent with epitaxial growth from the surviving Ni-20W crystal into the DD419 casting. At higher magnification, the interface appeared compact and continuous. However, optical images cannot establish whether thin oxide films or reaction products were present. A dark etched line was visible along part of the interface.

The observations show that orientation inheritance and local stray grains can coexist in the same seeding region. Similar studies of seed melt-back regions have shown that residual-solid morphology, interface conditions, and transient thermal fields influence the competition between inherited growth and other grains [8,9,20].

3.3. Crystallographic Orientation Transfer Across the Heterogeneous Interface

Laue X-ray diffraction was performed on the Ni-20W seed and the corresponding DD419 casting to assess crystallographic orientation inheritance in the plate-casting experiment. Figure 7 shows the paired measurements. The software-reported differences in Theta and Alpha were 0.2° and 2.7°, respectively, and the software-reported R value was 3.52. The paired Laue patterns and angular differences are consistent with orientation inheritance from the Ni-20W seed to the corresponding DD419 casting. The available

records do not specify the definition of R or a predefined acceptance threshold; therefore, the results are interpreted as descriptive evidence rather than a formal pass/fail assessment.

The result agrees with the established role of a partially unmelted seed as the crystallographic substrate for epitaxial growth during directional solidification [23].

In this plate specimen, the paired Laue measurements were consistent with orientation inheritance, while visible grain defects remained near the seed-casting transition region. Thus, a Ni-20W seed may provide a crystallographic template for epitaxial growth without ensuring a defect-free transition region.

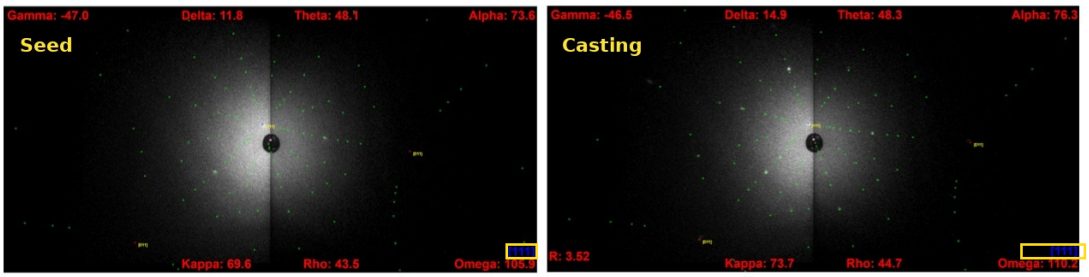


Figure 7. Laue X-ray diffraction measurements used to evaluate crystallographic orientation transfer from the Ni-20W seed to the corresponding DD419 casting. (**Left**): Ni-20W seed; (**right**): corresponding DD419 casting. The software-indexed [111] labels are highlighted in each pattern.

3.4. Comparison Between Ni-20W Heterogeneous and DD419 Homogeneous Seeds

Comparative turbine-blade casting experiments were conducted using Ni-20W heterogeneous seeds and DD419 homogeneous seeds in the same casting batch (Figure 8). After casting, the seed portions separated from all nine blades during shell removal, when mechanical vibration occurred. Macroscopic examination of the separated surfaces revealed black or gray oxide residues on both the seed and casting sides (Figure 9). Prolonged high-temperature exposure during directional solidification may promote oxidation at the seed surface. Previous studies have reported that oxide films formed during the seeding process can affect metallurgical bonding between the seed and the casting [19]. An oxide-containing interfacial layer may therefore have contributed to the separation, while mechanical vibration during shell removal may have triggered it.

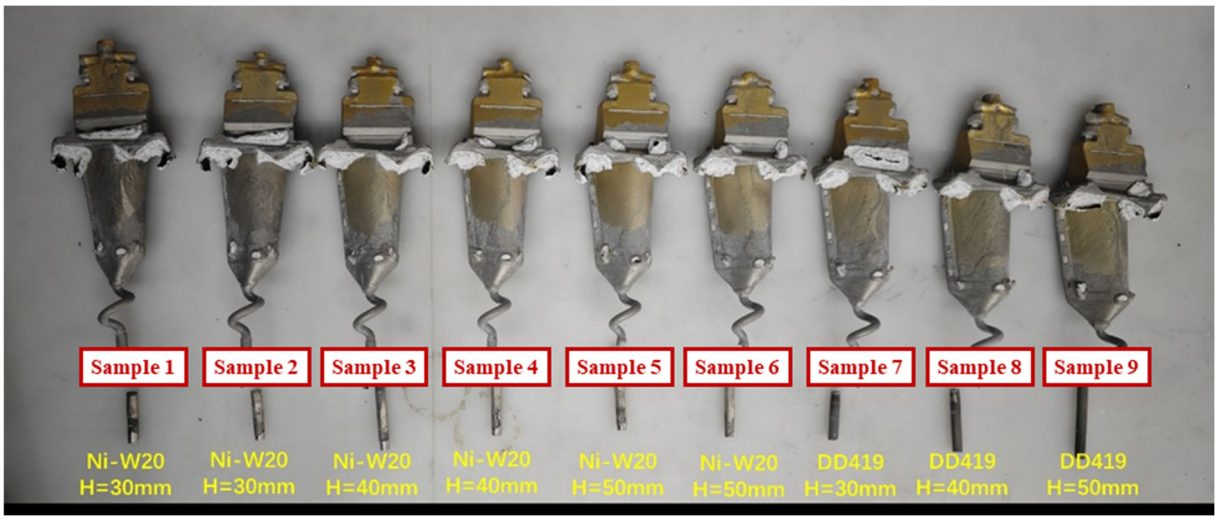


Figure 8. DD419 turbine-blade castings produced using Ni-20W heterogeneous seeds and DD419 homogeneous seeds with seed heights of 30, 40, and 50 mm. From left to right, Samples 1–6 were produced using Ni-20W seeds (two per height), and Samples 7–9 using DD419 seeds (one per

height). The detached seed portions are visible below the castings. The corresponding longitudinal sections of Samples 1, 3, 5, 7, 8, and 9 are shown in Figure 10a–f, respectively.

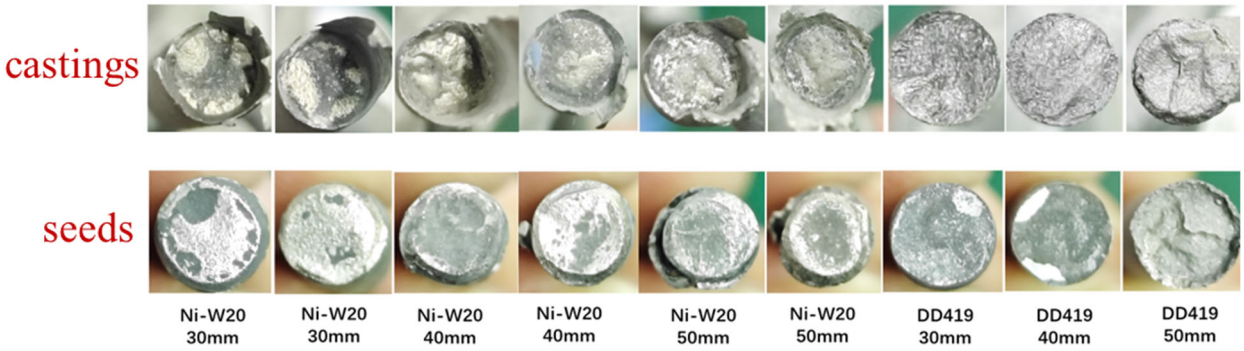


Figure 9. Macroscopic appearance of the blade castings (**top row**) and their corresponding detached seed portions (**bottom row**) after shell removal.



Figure 10. Macroetched grain structures of the starter regions of DD419 turbine-blade castings produced using Ni-20W heterogeneous seeds and DD419 homogeneous seeds at initial seed heights of 30, 40, and 50 mm: (**a**,**b**) Ni-20W, 30 mm; (**c**,**d**) Ni-20W, 40 mm; (**e**,**f**) Ni-20W, 50 mm; (**g**) DD419, 30 mm; (**h**) DD419, 40 mm; and (**i**) DD419, 50 mm. Each Ni-20W panel represents a separate blade casting. J marks the seed-selector junction at the separated end, and SG arrows point to local macroetched grain-contrast features identified as stray grains in the Ni-20W specimens.

After macroetching, the blade bodies appeared macroscopically single-crystalline away from the starter regions. Examination of the starter regions, however, revealed a pronounced difference between the two seed materials (Figure 10). Visible interfacial stray grains were observed near the seed-casting transition region in all six Ni-20W-seeded castings, and some extended upward into the grain-selector region. In contrast, no comparable interfacial stray grains were observed on the examined starter-region surfaces of the three DD419-seeded castings.

Longitudinal sections of the detached seeds showed different melt-back behavior (Figure 11). The melt-back lengths were measured directly using a metallographic microscope. The maximum measured melt-back lengths were approximately 12 mm for Ni-20W (specimen 3) and 45 mm for DD419 (specimen 9). One longitudinal section was examined for each of the six material-height combinations. The shorter maximum melt-back length observed for Ni-20W is consistent with its higher liquidus temperature, as measured in Section 3.1. The available records do not specify a separate image-analysis procedure, and replicate-based scatter cannot be estimated from these sections. The sections were cut approximately along the seed centerline, but the exact cutting-plane positions were not recorded. The remaining differences in visible section width are therefore not interpreted as differences in nominal seed diameter.

The blade comparison therefore shows that the two seed materials exhibited different melt-back behavior under the same casting schedule. The plate experiment, considered separately, shows that a surviving Ni-20W seed can transfer orientation into DD419. Together, the two experiments distinguish orientation-transfer capability from defect behavior in the blade starter region.

3.5. Factors Associated with Interfacial Stray-Grain Formation

These observations come from two different experiments and should be interpreted separately. In the plate specimen, metallography and paired Laue measurements were consistent with orientation inheritance from Ni-20W to DD419. In the blade batch, Ni-20W and DD419 seeds developed different melt-back states and different interfacial stray-grain morphologies. The key question is how the melt-back behavior of Ni-20W differs from that of the homogeneous seed under the same nominal casting schedule.

The clearest difference between the materials was their melt-back behavior. Ni-20W had a liquidus temperature of approximately 1493 °C, about 100 °C higher than that of DD419. Its maximum observed melt-back length was about 12 mm, compared with about 45 mm for DD419. These values indicate a shallower melt-back state for Ni-20W under the same nominal casting schedule. The schedule may require adjustment for the higher-liquidus heterogeneous seed. However, the present results do not establish whether the nominal furnace set point of 1520 °C and withdrawal rate of 3 mm min^{-1} are inherently mismatched for Ni-20W. Because local temperature gradients and instantaneous interface velocities were not measured, the 33 mm difference is an observed maximum-to-maximum comparison rather than a predictive heat-balance estimate.

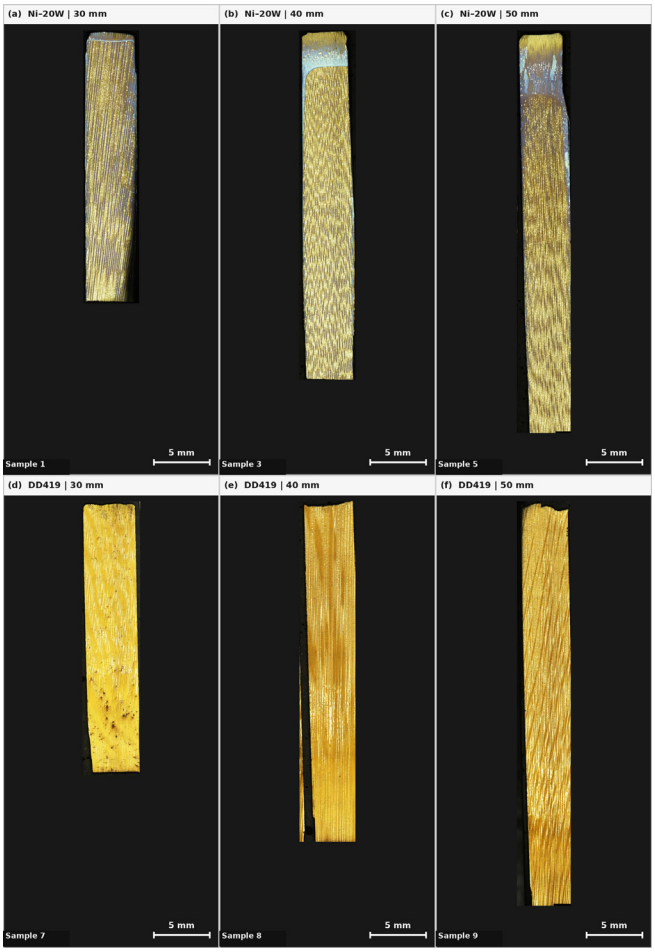


Figure 11. Longitudinal optical micrographs showing the melt-back behavior of Ni-20W and DD419 seeds: (**a**) Sample 1, 30 mm Ni-20W seed; (**b**) Sample 3, 40 mm Ni-20W seed; (**c**) Sample 5, 50 mm Ni-20W seed; (**d**) Sample 7, 30 mm DD419 seed; (**e**) Sample 8, 40 mm DD419 seed; (**f**) Sample 9, 50 mm DD419 seed. The nominal diameter of each seed was 7 mm. The panels retain the physical top-to-bottom seed orientation.

Ni-20W also exhibited a lower critical nucleation undercooling. In both thermal cycles, ΔT_N was 14.5 °C for Ni-20W, compared with 44 and 37 °C for DD419. Previous work has linked lower undercooling capacity with greater stray-grain susceptibility in single-crystal superalloy castings [22]. In the present study, this material characteristic is consistent with the stray grains observed during Ni-20W seed preparation. The 14.5 °C value characterizes the Ni-20W thermal-analysis specimen; it is not a direct measurement of the local liquid at the Ni-20W/DD419 interface. This association does not establish that the measured bulk undercooling caused the interfacial stray grains in the blade castings.

Previous studies have linked stray-grain formation near the seed melt-back region to residual-solid morphology, transient thermal fields, seed-mold clearance, and oxide-related effects [8,9,18–21]. In particular, the original primary dendrite spacing can affect the connectivity of residual solid during partial melt-back. A finer initial spacing has been reported to promote a connected solid network rather than isolated dendrite stems, thereby suppressing stray-grain formation [8,9]. In the present blade comparison, Ni-20W exhibited a higher liquidus temperature and a shorter maximum melt-back length than DD419 under the same nominal casting schedule. This difference may have produced different residual-solid configurations near the interface. The lower critical nucleation undercooling measured for Ni-20W is also consistent with a greater susceptibility to nucleation, although it does not represent the local liquid condition at the seed-casting interface.

The local temperature gradient and interface growth velocity evolve during initial seeding and jointly affect the development of constitutional undercooling ahead of the advancing interface [17,20]. Solute redistribution between Ni-20W and DD419 may further alter the local liquidus and growth conditions. The local growth direction relative to the crystallographic orientation may also influence competition between inherited growth and competing grains. Qin et al. [17] reported fine cellular grains at Ni-W remelting interfaces under high-rate solidification, but not under liquid-metal-cooling conditions. The macroetched interfacial stray grains observed in the present blade castings cannot be assumed to be the same cellular structures because their local crystallographic orientations and compositions were not measured. These factors therefore provide possible explanations for the observed differences, but their individual contributions remain unresolved.

The plate Laue results are consistent with Ni-20W providing a crystallographic template for epitaxial growth. In the blade comparison, however, Ni-20W showed less melt-back but more visible interfacial stray grains than DD419 under the same nominal schedule. Orientation-transfer capability and defect-free seeding should therefore be treated as separate performance criteria. Future work could evaluate a higher furnace temperature, a lower withdrawal rate, modified seed geometry, or an intermediate buffer layer to assess their effects on interfacial reliability.

4. Conclusions

(1) Ni-20W exhibited a higher liquidus temperature and lower critical nucleation undercooling than DD419. In two thermal cycles, the liquidus temperatures of Ni-20W were 1492.6 and 1493.6 °C, and ΔT_N was 14.5 °C in both cycles. DD419 had liquidus temperatures of 1388.8 and 1394.1 °C, with ΔT_N values of 44 and 37 °C.

(2) In one of the two plate castings, the paired Laue patterns and angular differences were consistent with orientation inheritance from Ni-20W to DD419. The software-reported differences in Theta and Alpha were 0.2° and 2.7°, respectively, and the R value was 3.52.

(3) In the same-batch blade comparison, the maximum observed melt-back lengths were approximately 12 mm for Ni-20W and 45 mm for DD419. Visible interfacial stray grains were found on the examined starter-region surfaces of all six Ni-20W-seeded blades; no comparable features were observed on the examined surfaces of the three DD419-seeded blades.

(4) These results distinguish orientation-transfer capability from defect-free heterogeneous seeding. Under the investigated casting conditions, the paired Laue data were consistent with orientation inheritance in the plate specimen, whereas the blade comparison showed less melt-back and more visible interfacial stray grains for Ni-20W than for DD419 homogeneous seeds. Process optimization specific to the heterogeneous seed may be needed to improve interfacial reliability.

Author Contributions: Conceptualization, X.G.; Methodology, X.G., M.L., C.C., J.W., W.X. and Y.D.; Software, M.L., Y.Z., J.W., W.X. and Y.D.; Validation, X.G., M.L., C.C., J.W. and W.X.; Formal analysis, C.C., J.W. and L.L.; Investigation, M.L., Y.Z., J.W., L.L. and Y.D.; Data curation, C.C., Y.Z., W.X., L.L. and Y.D.; Writing—original draft, X.G. and L.L.; Writing—review & editing, X.G., C.C. and D.M.; Visualization, Y.Z. and Y.D.; Supervision, C.C. and D.M.; Project administration, D.M.; Funding acquisition, D.M. All authors have read and agreed to the published version of the manuscript.

Funding: This research was supported by the Shenzhen Science and Technology Program (JSGG20220831092800001) and the Guangdong Innovative and Entrepreneurial Research Team Program (607264877417).

Data Availability Statement: The data presented in this study are available from the corresponding author upon reasonable request.

Conflicts of Interest: Authors Xiaoyi Gong, Yunxing Zhao, Dexin Ma, Jianhui Wei, Weitai Xu, Lv Li and Yangpi Deng were employed by the company Shenzhen Wedge Aviation Technology Co., Ltd. The remaining authors declare that the research was conducted in the absence of any commercial or financial relationships that could be construed as a potential conflict of interest.

References

1. Higginbotham, G.J.S. From research to cost-effective directional solidification and single-crystal production—An integrated approach. Part A—Process development. *Mater. Des.* **1986**, *7*, 237–245. https://doi.org/10.1016/0261-3069(86)90048-8.
2. Xu, M.; Zhang, X.; Geng, X.; Liu, G.; Wang, Y.; Wang, Z.; Guo, J.; Wang, G. Study on the formation and competitive growth mechanism of stray grains during spiral grain selector of nickel-based single crystal superalloy. *Mater. Lett.* **2021**, *294*, 129747. https://doi.org/10.1016/j.matlet.2021.129747.
3. Dai, H.J.; D'Souza, N.; Dong, H.B. Grain selection in spiral selectors during investment casting of single-crystal turbine blades: Part I. Experimental investigation. *Metall. Mater. Trans. A* **2011**, *42*, 3430–3438. https://doi.org/10.1007/s11661-011-0760-6.
4. Dai, H.J.; Dong, H.B.; D'Souza, N.; Gebelin, J.-C.; Reed, R.C. Grain selection in spiral selectors during investment casting of single-crystal components: Part II. Numerical modeling. *Metall. Mater. Trans. A* **2011**, *42*, 3439–3446. https://doi.org/10.1007/s11661-011-0757-1.
5. Stanford, N.; Djakovic, A.; Shollock, B.A.; McLean, M.; D'Souza, N.; Jennings, P.A. Seeding of single crystal superalloys—Role of seed melt-back on casting defects. *Scr. Mater.* **2004**, *50*, 159–163. https://doi.org/10.1016/j.scriptamat.2003.08.029.
6. Stanford, N.; Djakovic, A.; Shollock, B.A.; McLean, M.; D'Souza, N.; Jennings, P.A. Defect grains in the melt-back region of CMSX-4 single crystal seeds. In *Superalloys 2004*; Green, K.A., Pollock, T.M., Harada, H., Howson, T.E., Reed, R.C., Schirra, J.J., Walston, S., Eds.; TMS: Warrendale, PA, USA, 2004; pp. 719–726. https://doi.org/10.7449/2004/Superalloys_2004_719_726.
7. Hallensleben, P.; Schaar, H.; Thome, P.; Jöns, N.; Jafarizadeh, A.; Steinbach, I.; Eggeler, G.; Frenzel, J. On the evolution of cast microstructures during processing of single crystal Ni-base superalloys using a Bridgman seed technique. *Mater. Des.* **2017**, *128*, 98–111. https://doi.org/10.1016/j.matdes.2017.05.001.
8. Hu, S.; Liu, L.; Yang, W.; Sun, D.; Huo, M.; Li, Y.; Huang, T.; Zhang, J.; Su, H.; Fu, H. Inhibition of stray grains at melt-back region for re-using seed to prepare Ni-based single crystal superalloys. *Prog. Nat. Sci. Mater. Int.* **2019**, *29*, 582–586. https://doi.org/10.1016/j.pnsc.2019.08.006.
9. Hu, S.; Yang, W.; Li, Z.; Xu, H.; Huang, T.; Zhang, J.; Su, H.; Liu, L. Formation mechanisms and control method for stray grains at melt-back region of Ni-based single crystal seed. *Prog. Nat. Sci. Mater. Int.* **2021**, *31*, 624–632. https://doi.org/10.1016/j.pnsc.2021.07.004.
10. Ford, D.A.; Hill, A.D. Single Crystal Seed Alloy. U.S. Patent 6,740,176 B2, 25 May 2004.
11. Azhazha, V.M.; Gorbenko, Y.V.; Kovtun, G.P.; Ladygin, A.N.; Malykhin, D.G.; Rudycheva, T.Y.; Sverdlov, V.Y.; Shcherban, A.P.; Zhemanyuk, P.D.; Klochikhin, V.V. The growth of single crystals of Ni–W alloy under conditions of high temperature gradient. *Crystallogr. Rep.* **2004**, *49*, 307–311. https://doi.org/10.1134/1.1690436.
12. Azhazha, V.M.; Ladygin, A.N.; Sverdlov, V.J.; Zhemanyuk, P.D.; Klochikhin, V.V. Morphological transition in the cellular structure of single crystals of nickel–tungsten alloys near the congruent melting point. *Crystallogr. Rep.* **2005**, *50*, S130–S135. https://doi.org/10.1134/1.2133988.
13. Azhazha, V.M.; Sverdlov, V.Y.; Ladygin, A.N.; Shcherban, A.P.; Boguslaev, A.V.; Klochikhin, V.V. Self-organization processes in the cellular structure formation of Ni–W alloys. *J. Surf. Investig. X-Ray Synchrotron Neutron Tech.* **2008**, *2*, 156–165. https://doi.org/10.1007/s11700-008-1025-x.
14. Toloraiya, V.N.; Orekhov, N.G.; Kablov, E.N. Advanced method for single crystal casting of turbine blades for gas turbine engines and plants. *Metal. Sci. Heat Treat.* **2002**, *44*, 279–283. https://doi.org/10.1023/A:1021299619346.
15. Zhao, N.; Li, J.; Liu, J.; Wang, Z.; Jin, T.; Sun, X.; Guan, H.; Yang, H.; Hu, Z. Solidification interface in growth of single crystal superalloys by seeding technique. *J. Mater. Eng.* **2007**, *11*, 24–27.
16. Guo, J.; Li, J.; Liu, J.; Huang, J.; Meng, X.; Sun, X. Formation mechanism of fusion zone in growth of single crystal superalloy with low-segregated heterogeneous seed. *Acta Metall. Sin.* **2018**, *54*, 419–427. https://doi.org/10.11900/0412.1961.2017.00144. (In Chinese).

17. Qin, J.; Yang, W.; Qu, P.; Liu, C.; Zhang, J.; Liu, L. Microstructure on remelting interface of Ni–W heterogeneous seed in preparing Ni-based single crystal superalloys. *J. Mater. Res. Technol.* **2021**, *12*, 264–270. https://doi.org/10.1016/j.jmrt.2021.02.086.
18. Deng, Y.; Ma, D.; Wei, J.; Zhao, Y.; Li, L.; Cheng, B.; Xu, F. Formation mechanisms of chilled layer on the perimeter of superalloy seed. *Metals* **2026**, *16*, 79. https://doi.org/10.3390/met16010079.
19. Cheng, B.; Li, L.; Ma, D.; Wei, J.; Zhao, Y.; Deng, Y.; Xu, F. Impact of the oxide film formed during the seeding process of single-crystal superalloys. *Metals* **2026**, *16*, 834. https://doi.org/10.3390/met16080834.
20. Hu, S.; Zhao, Y.; Bai, W.; Wang, X.; Yin, F.; Yang, W.; Liu, L. Temperature field evolution of seeding during directional solidification of single-crystal Ni-based superalloy castings. *Metals* **2022**, *12*, 817. https://doi.org/10.3390/met12050817.
21. Zhang, Y.; Wang, D.; Zhang, J. Oxygen-induced stray grain formation in nickel-based single crystal superalloys. *J. Alloys Compd.* **2026**, *1055*, 186429. https://doi.org/10.1016/j.jallcom.2026.186429.
22. Ma, D.; Zhao, Y.; Xu, W.; Xu, F.; Wei, J.; Zhang, H. Comparative investigation of the undercooling capacity and single-crystal castability of some Ni-based superalloys. *Crystals* **2023**, *13*, 57. https://doi.org/10.3390/cryst13010057.
23. Yang, S.; Bao, J.; Yang, X.; Zheng, Q.; Liu, Q.; Zhang, J.; Hu, S. Controlling crystal orientation of Ni-based single crystal superalloy by inclined seeding method. *J. Mater. Eng.* **2025**, *53*, 63–69. https://doi.org/10.11868/j.issn.1001-4381.2024.000025.
24. Xu, W.; Ma, D.; Zhao, Y.; Pi, L.; Sun, Z. Investigation on the undercoolability and solidification structure of some single crystal superalloys. *Rare Metal. Mater. Eng.* **2022**, *51*, 2637–2644. https://rmme.ijournals.cn/rmme/article/html/20210552.
25. Li, Q.; Xie, J.; Yu, J.J.; Shu, D.; Hou, G.; Sun, X.; Zhou, Y. Solidification behavior and segregation characteristics of high W-content cast Ni-based superalloy K416B. *J. Alloys Compd.* **2021**, *854*, 156027. https://doi.org/10.1016/j.jallcom.2020.156027.
26. Zhang, L.; Huang, Z.; Jiang, L.; Luan, J.; Jiao, Z.; Liu, C.T. Effect of Mo:W ratio on segregation behavior and creep strength of nickel-based single crystal superalloys. *Mater. Sci. Eng. A* **2019**, *744*, 481–489. https://doi.org/10.1016/j.msea.2018.12.043.

Disclaimer/Publisher's Note: The statements, opinions and data contained in all publications are solely those of the individual author(s) and contributor(s) and not of MDPI and/or the editor(s). MDPI and/or the editor(s) disclaim responsibility for any injury to people or property resulting from any ideas, methods, instructions or products referred to in the content.